Report: Cornell ERL-04-2

# Reducing the Synchrotron Radiation on RF Cavity Surfaces in the proposed Cornell Energy-Recovery Linac

G. H. Hoffstaetter*, T. Tanabe

February 8, 2004

## Abstract

It has been suggested to build a synchrotron-light facility based on an Energy-Recovery LINAC (ERL) at Cornell University. For this purpose, it was investigated to what extent the CESR facilities could be reused. For this the LINAC must be segmented in sections that are connected by bends. While there are unexpected advantages to this design, we are here analyzing the synchrotron radiation that is produced in these bending sections and that can heat the surface of the superconducting cavities of the following linac section. In particular, we investigate how the synchrotron radiation load on the superconducting niobium RF cavities can be reduced.

## 1 Introduction

In the calculations that study an ERL in Cornell's CESR tunnel, the superconducting niobium RF cavities are placed a few meters after the bending section [1], as shown in Fig. 1. The synchrotron radiation produced by high energy electrons propagates outward in a bending magnet, hitting the surface of the RF cavities. This is not desirable since the accumulation of radiation would result in high enough temperature to produce breakdown of superconductivity. Furthermore, it produces photo-emitted electrons which can be accelerated and produce a dark current heat load. In this paper, we investigate the amount of radiation on the RF cavities, and analyze how it can be reduced.

## 2 Synchrotron Radiation

The radiated power created per unit length of a bending magnet by a beam current $I$ with particles of charge $q$ and mass $m$ is given by

$$\frac{dP_{tot}}{dl} = \frac{q}{6\pi\epsilon_0}\frac{\beta^3}{(mc^2)^4}\frac{IE^4}{\rho^2} \ . \tag{1}$$

*Georg.Hoffstaetter@cornell.edu

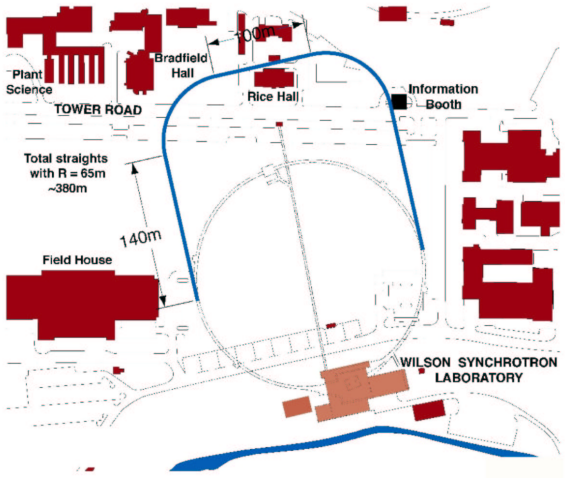


Figure 1: An ERL in an extended CESR tunnel.

The energy of the particles is $E$ and $\rho$ is the bending radius in the magnet. In reasonable units, one obtains [2]

$$\frac{dP_{tot}}{dl}\left[\frac{\mathrm{kW}}{\mathrm{m}}\right] = 14.097\frac{\mathrm{kW}}{\mathrm{m}}\cdot\frac{I\cdot E^4}{\rho^2}\left[\frac{\mathrm{m}^2}{\mathrm{A(GeV)}^4}\right] = \frac{C_0}{\rho^2} \ , \tag{2}$$

where in the following evaluations $C_0 = 155.0\mathrm{Wm}$ for a current of 100mA and an energy of 3.238GeV, which is the energy of the second bend in the linac region of Fig. 1. The four-dimensional power distribution of a Gaussian distributed particle beam is given by [2]:

$$\begin{aligned}\frac{dP}{dl}(x,x',y,y') = \frac{C_0}{4\pi^2\epsilon_x\epsilon_y}&\left\{\left(\frac{1}{\rho}+Kx\right)^2+K^2y^2\right\}\\ &\times\exp\left(-\frac{\gamma_x x^2+2\alpha_x xx'+\beta_x x'^2}{2\epsilon_x}\right)\\ &\times\exp\left(-\frac{\gamma_y y^2+2\alpha_y yy'+\beta_y y'^2}{2\epsilon_y}\right)\end{aligned} \tag{3}$$

Here, $\alpha_{x,y}$, $\beta_{x,y}$, and $\gamma_{x,y}$ are the Twiss parameters defined as $\alpha_{x,y} = -\beta'_{x,y}/2$ and $\gamma_{x,y} = (1+\alpha^2_{x,y})/\beta_{x,y}$.

These are not to be confused with the relativistic factors which are denoted by $\beta$ and $\gamma$ without subscript.

To include the $1/\gamma$ spread of the radiation [3], we approximate the angular divergence of synchrotron radiation of an individual particle by a Gaussian with standard deviation of $1/\gamma$, and take the convolution with the power formula:

$$\begin{aligned}
&\frac{dP_\gamma}{dl}(x,y,x',y') = \int_{-\infty}^{\infty}\int_{-\infty}^{\infty} \frac{dP}{dl}(x,y,x'-\xi,y'-\zeta) \\
&\times \left\{ \frac{1}{2\pi(1/\gamma)^2} \exp\left( -\frac{\xi^2+\zeta^2}{2(1/\gamma)^2} \right) \right\} d\xi\, d\zeta \\
&= \frac{C_0}{4\pi^2 \tilde{\epsilon}_x \tilde{\epsilon}_y} \left\{ \left( \frac{1}{\rho} + Kx \right)^2 + K^2 y^2 \right\} \\
&\times \exp\left( -\frac{\tilde{\gamma}_x x^2 + 2\tilde{\alpha}_x x x' + \tilde{\beta}_x x'^2}{2\tilde{\epsilon}_x} \right) \\
&\times \exp\left( -\frac{\tilde{\gamma}_y y^2 + 2\tilde{\alpha}_y y y' + \tilde{\beta}_y y'^2}{2\tilde{\epsilon}_y} \right) .
\end{aligned} \tag{4}$$

Here we redefined the constants as

$$\tilde{\alpha}_{x,y} = \frac{\alpha_{x,y}}{\mu_{x,y}} , \quad \tilde{\beta}_{x,y} = \frac{\beta_{x,y}}{\mu_{x,y}} \tag{5}$$

$$\tilde{\gamma}_{x,y} = \frac{\gamma_{x,y} + \frac{1}{\gamma^2 \epsilon_{x,y}}}{\mu_{x,y}} , \quad \tilde{\epsilon}_{x,y} = \mu_{x,y}\, \epsilon_{x,y} \tag{6}$$

$$\mu_{x,y} = \sqrt{1 + \frac{\beta_{x,y}}{\gamma^2 \epsilon_{x,y}}} . \tag{7}$$

# 3 Computational Tool

Using Eq. (4), we have developed a computer program that computes the propagation of synchrotron radiation numerically by propagating the radiation from different magnet slices to a screen as indicated in Fig. 2. To investigate cavity walls, the code is written so that the screen can have an arbitrary angle to the optical axis. We use BMAD [4] to calculate the Twiss parameters at any point in the trajectory of the beam, given the lattice of the ERL.

We then slice each magnet into many small pieces and project the synchrotron radiation to a planar screen placed at a certain distance. At this screen we sum the power $\Delta P$ that is radiated by all small slices of width $\Delta l$ by $\Delta P = \frac{C_0}{\rho^2}\Delta l$.

As an example, Fig. 3 shows the radiation density at a screen that is perpendicular to the cavity axis and directly at the entrance of the first cavity, 2.5m after the bending magnet. The maximum radiation density is too large and has to be reduced.

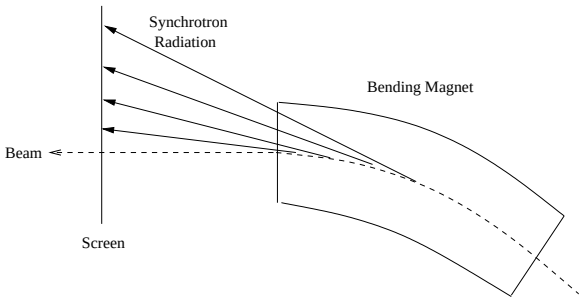


Figure 2: Propagating synchrotron radiation.

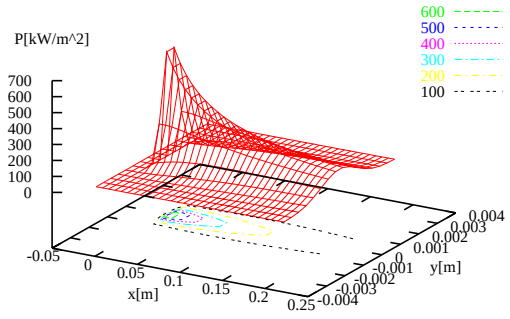


Figure 3: Radiation profile at the cavity entrance.

If one introduces shielding of the radiation, our formula Eq. (4) no longer works since it assumes that no object is present in the pathway of the radiation. If there is such an object, the limits of the integrals in Eq. (4) will have to be adjusted, which gives a complicated formula that depends on the geometry. This method is inefficient because the calculation cannot be generalized.

To overcome this, we modified our program to use the four-dimensional power distribution Eq. (3) if any shielding material is present. In this approach, the program tests if the beam hits a shield for sufficiently many particles with different positions and angles. If so, it propagates the 4-dimensional distribution to the plane of the obstacle. Our program supports an arbitrary number of apertures. We assumed that the radiation that hits an aperture is completely absorbed. Reflections and secondary particles are not taken into account.

# 4 Radiation on Cavity Surface

In this section, we compute some analytical estimates of the radiation power. Some relevant distances are introduced in Fig. 4.

After the beam comes out of the last bending magnet

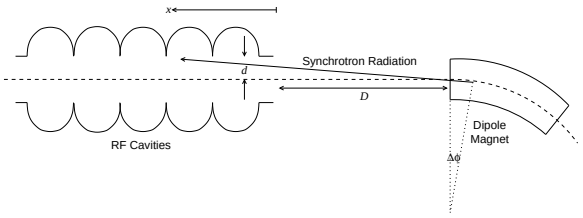


Figure 4: Radiation from dipole to cavity.

of the arc in Fig. 1, it transverses a drift distance $D$ and then enters the cavities as shown in Fig. 4. We investigate the radiation on a circular tube of radius $d$ that is meant to approximate the cavity wall.

| Parameter | Value |
|---|---|
| $\rho$ [m] | 77 |
| $d$ [m] | .035 |
| $D$ [m] | 2.5 |
| $I$ [A] | .1 |
| $E$ [GeV] | 3.238 |
| $C_0$ [kWm] | 155.0 |

Table 1: Parameters of the ERL bend.

The linear radiation power density that shines on this cylindrical cavity surface at a distance $x$ after the start of the linac section is denoted by $\frac{d}{dx}P$. To compute this power density, we need to find the angle $\Delta\phi$ of the ray originating from a point in the arc and hitting the end of the section at $x$. As shown in Fig. 4, $\Delta\phi$ is also the angle between the ray and the cavity axis,

$$\tan\Delta\phi = \frac{h(\Delta\phi)}{L(\Delta\phi)} , \quad (8)$$

$$h(\Delta\phi) = d + \rho\,(1-\cos\Delta\phi) , \quad (9)$$

$$L(\Delta\phi) = D + x + \rho\sin\Delta\phi . \quad (10)$$

To first order in $\Delta\phi$ this leads to

$$\Delta\phi = \frac{d}{D+x} . \quad (11)$$

A second order expansion $\Delta\phi$ leads to

$$\Delta\phi(x) = \frac{D+x}{\rho}\left[\sqrt{1+\frac{2d\rho}{(D+x)^2}}-1\right] . \quad (12)$$

The first order approximation is therefore only valid for $d\rho \ll (D+x)^2$, which is not valid for the parameters of Tab. 1. The total power $P$ radiated into the cavity is given by

$$P_{total} = \frac{C_0}{\rho}\Delta\phi(0) . \quad (13)$$

For the parameters in Tab. 1 this is 24W. The power irradiating the cylindrical wall before $x$ is

$$P(x) = P_{total} - \frac{C_0}{\rho}\Delta\phi(x) \quad (14)$$

Finally, the linear power density is

$$\frac{d}{dx}P = \frac{C_0}{\rho^2}\left\{1-\left[1+\frac{2d\rho}{(D+x)^2}\right]^{-\frac{1}{2}}\right\} . \quad (15)$$

In Fig. 5 (top) the first (dark blue) and second (light green) order estimation are compared. The first order treatment is obviously not sufficient. The second order treatment, however, agrees well with the numerical propagation of the radiation by Eq. (4) in Fig. 5 (bottom).

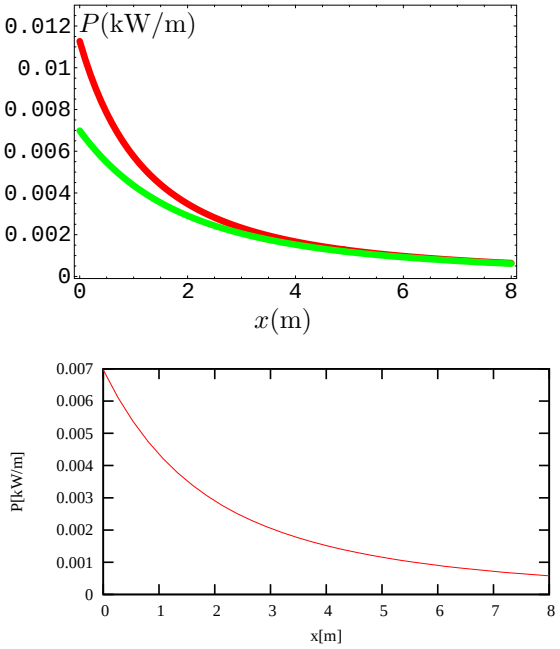


Figure 5: Linear power density along the cylindrical cavity surface. Top: approximation with first order (dark blue) and second order (light green) treatment. Bottom: numerical radiation propagation.

Assuming uniform radiation within an opening angle of $2/\gamma$, the radiation per area on the cylindrical cavity wall is approximately

$$\frac{d}{da}P = \frac{d}{dx}P\frac{\gamma}{2L(\Delta\phi(x))} = \frac{\gamma C_0 d}{2\rho}\frac{\Delta\phi(x)}{(D+x)^2+2d\rho} , \quad (16)$$

which is shown in Fig. 6. While this is already a very large radiation load compared to the static heat load of about $50W/m^2$ of the planed cavities. However, as indicated in Fig. 4, the cavity has surfaces that are nearly

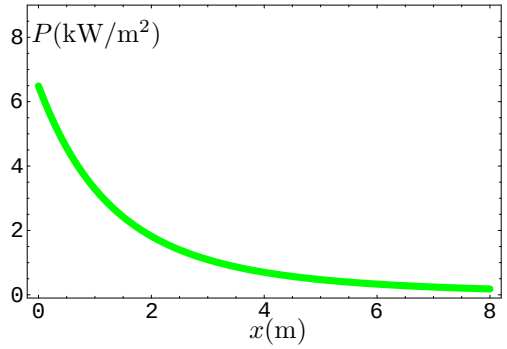


Figure 6: Radiation per area on the cylindrical cavity surface.

perpendicular to the radiation direction. At these surfaces the radiation density is larger by $1/\tan\Delta\phi$, leading to a worst case radiation density at the cavity wall of

$$\frac{d}{da}P_\perp = \frac{d}{da}P\frac{1}{\Delta\phi(x)} = \frac{\gamma C_0 d}{2\rho}\frac{1}{(D+x)^2+2d\rho}\,, \quad (17)$$

which is plotted in Fig. 7.

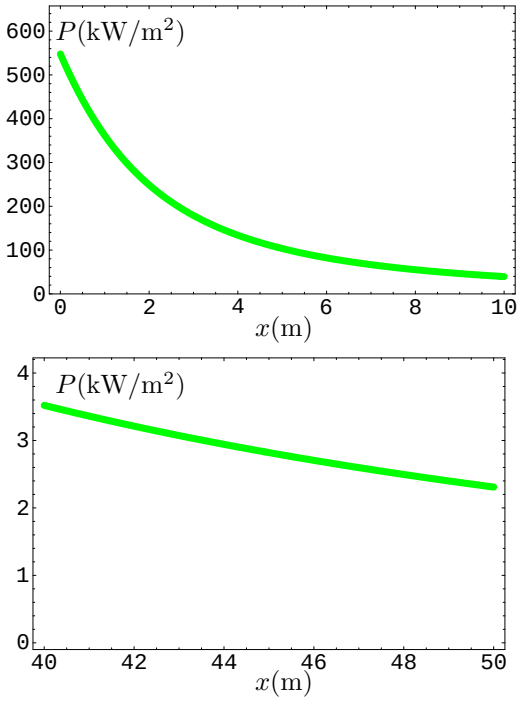


Figure 7: Radiation per area on an exposed cavity surface that is perpendicular to the radiation direction: close to the entrance of the linac (top) and near the center of the linac section (bottom).

It should be noted that the cavity surface is not perpendicular to the radiation direction, since most of the surface of a cell is shielded by the previous iris. Therefore only regions close to the irises can be irradiated, as shown in Fig. 8.

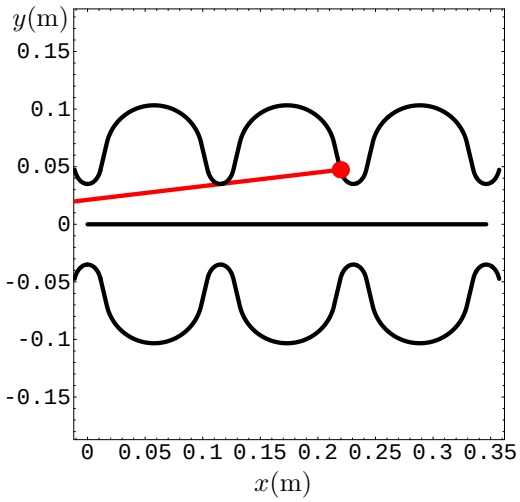


Figure 8: Radiation inside a cavity.

The cavity is made out of shells [5] with circular, straight, or elliptical sections as shown in Fig. 9. The periodicity of the cavity cells is $L = 57.692$mm, the center of the circles are located at $(x_c, y_c) = (2nL, \pm 61.3\mathrm{mm})$ and the center of the ellipses are located at $(x_e, y_e) = \left(\left(n+\frac{1}{2}\right)57.692, \pm 54\mathrm{mm}\right)$. The radius of the circles is 42mm and the horizontal and vertical main axes of the ellipses are $a = 12$mm and $b = 19$mm. Neighboring ellipses and circles are connected by a straight line. The onset of this straight line at the ellipse is at $(x_e, y_e) + (-a\sin\phi_0, -b\cos\phi_0)$ with $\phi_0 = 1.212899$.

It turns out that radiation with an angle to the optical axis of less than an angle $\theta_m$ only reaches the elliptical iris section and not the straight section. This angle is given by the following formula where $c(\theta_0) = \cos(\theta_0) + \frac{r_1 - r_2}{b}$ and the radii of two successive irises are $r_1$ and $r_2$, while the irises are a distance $L$ apart,

$$\sin\theta_m = \frac{\frac{L}{a} - \sin\phi_0 - c(\phi_0)\sqrt{(\frac{L}{a}\sin\phi_0 - 1)^2 + c(\phi_0)^2 - 1}}{(\frac{L}{a} - \sin\phi_0)^2 + c(\phi_0)^2}\,. \quad (18)$$

Within a cavity one has $r_1 = r_2 = 35$mm and very large incident angles of $\theta \geq \theta_m^{(1)} = 0.1185$ are required to irradiate the straight section between iris and equator. The first iris in each cavity has $r_1 = 39mm$ and one obtains $\theta_m^{(2)} = 0.0802$.

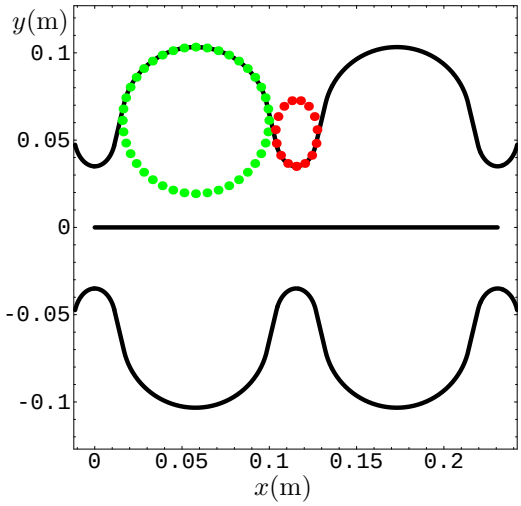


Figure 9: Geometrical structure of TESLA cavities [5].

The slope of the elliptic section can then easily be computed and it can be derived how much larger the power per area is on the straight or elliptical section of the cavity than on the cylindrical beam pipe. While the power on the perpendicular section is enhanced by $1/\tan(\theta)$, on the elliptical iris the enhancement is only proportional to $1/\sqrt{\theta}$ for small angles.

The radiation density along the linac is shown for the first two unequal irises and for irises inside the cavity in Fig. 10.

While these power densities are significantly smaller than those for perpendicular radiation in Fig. 7, they are still large for a superconducting environment. The question arises which power density a superconducting surface can tolerate.

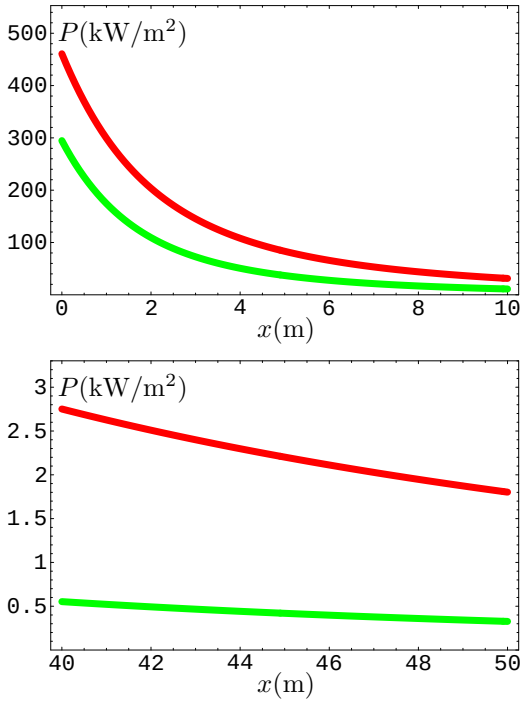


Figure 10: Radiation per area on an exposed cavity surface that has the correct slope on the elliptical iris section. Computed for the second iris, in the shadow of the first larger iris (dark blue) and for an iris inside a multi cell TESLA cavity (light green).

# 5 Tolerable Power Densities

## 5.1 Heating

Here we assume that the superconducting cavity is covered in a 2K Helium bath. The niobium, however, has a higher temperature for two reasons. (a) There is energy deposited in the niobium due to RF fields and the resistivity of the material, and (b) there is a Kapitza conductance that leads to a temperature jump at the surface between superconductor and helium. The AC surface resistance $R(T)$ of niobium strongly increases with temperature, so that the deposition of synchrotron radiation not only increases the power deposition, but it increases the temperature and thus the power that is absorbed from the RF field. This in turn increases the temperature again, leading to further power absorption.

The radiation power density $P_s$ plus the absorbed RF power $\frac{1}{2}R(T)H^2$ at a magnetic field $H$ constitute the total absorbed power $P$, which in turn determines the temperature $T(P)$,

$$P_s + R(T(P))\frac{1}{2}H^2 = P \ . \tag{19}$$

This implicit equation has to be solved for $P$, which leads to the temperature $T(P)$ at the vacuum side of the niobium, and the head transport equation leads to the temperature at the helium side of the material.

Programs are available that perform this procedure [6]. Results are shown in Tab. 2, where a magnetic field at the surface of $H$ =840Oe (6.7T) was assumed, corresponding to 20MV/m accelerating field. The last row

| $P_s$ | $T_{Nb}$(He) | $T_{Nb}$(Vac.) | $P$ |
|---|---|---|---|
| 1.0kWm$^{-2}$ | 2.46K | 2.74K | 1.43kWm$^{-2}$ |
| 2.0kWm$^{-2}$ | 2.58K | 2.96K | 2.60kWm$^{-2}$ |
| 2.3kWm$^{-2}$ | 2.62K | 3.02K | 3.01kWm$^{-2}$ |

Table 2: Niobium Temperature for helium at 2K.

of this table describes the maximum tolerable radiation power of 2.3kWm$^{-2}$. With slightly more synchrotron radiation power, the temperature increase becomes unstable so that no implicit solution $P$ exits. It has to be noted that this is a conservative estimate of the tolerable synchrotron power, since the areas with largest $H$ are close to the equator and are therefore not irradiated.

Short bunches emit a significant part of their radiation spectrum coherently, leading to strongly enhanced radiation power. For a Gaussian longitudinal bunch profile with bunch length $\sigma_\tau$ this leads to an increase in the total emitted power of [7]

$$\frac{P^{(N)}_{coh}}{P^{(N)}_{incoh}} = 0.002237\frac{GeV^4}{pC}\left(\frac{\mathrm{mm}}{\mathrm{m}}\right)^{\frac{4}{3}}\frac{q_{bunch}}{E^4}\left(\frac{\rho}{\sigma_\tau}\right)^{\frac{4}{3}} \ , \tag{20}$$

For a bunch length of 0.6mm and a bunch current of 77pC this leads to quite significant coherent synchrotron radiation as shown in Tab. 3 for the bending radii which are used in this study. For the shielding factor of the vacuum pipe we use a formula that has not been derived for a Gaussian longitudinal profile but for a uniform distribution of length $\sigma_\tau$,

$$k_{shield} = \left(\frac{\sigma_\tau}{\sqrt{3}\rho}\right)^{\frac{1}{3}}\frac{a}{2\sigma_\tau} \ . \tag{21}$$

For the distance between the shielding vacuum walls parallel to the plane of the orbit we use $a = 2$cm.

For the large bending radii the radiation is completely dominated by CSR and an enhancement of 86 is possible, which leads to a total power enhancement of only 4.9 due to shielding of CSR by a rather tight vacuum pipe. In the remainder of this report, only the incoherent part of the radiation is computed and plotted since the coherent radiation is in the infrared and has a much larger opening angle than the incoherent radiation. Furthermore it reflects very well off the niobium walls [9]. For the planned bunch-length of 0.6mm, coherent radiation is enhanced in the region of $\nu = \frac{c}{\sigma_\tau} = 500$GHz. At these frequencies the reflectivity is very close to 100% and the coherent radiation is therefore distributed over the total cavity area.

| $\rho$[m] | $\frac{P^{(N)}_{coh}}{P^{(N)}_{incoh}}$ | $k_{shield}$ | $\frac{P^{(N)}_{tot}}{P^{(N)}_{incoh}}$ |
|---|---|---|---|
| 45 | 0.50 | 0.33 | 1.16 |
| 77 | 1.01 | 0.28 | 1.28 |
| 393 | 8.9 | 0.08 | 1.71 |
| 1291 | 43.5 | 0.05 | 3.34 |

Table 3: Parameters of the ERL bend.

According to [9], photons that are incident on a superconducting surface can break Cooper pairs and therefore destroy superconductivity. For superconducting niobium the photon-energy threshold for this process is about 750GHz or $\lambda_{cut} = 0.4$mm. At this frequency the reflectivity jumps to about 98% and slowly increases with increasing frequency.

## 5.2 Electron Emission

The synchrotron radiation can also lead to emission of electrons from the niobium, which in turn can be accelerated and can damage vacuum components. For the parameters of Tab. 1, the characteristic photon energy is $E_c = \hbar\omega_c = \frac{3c\gamma^3}{2\rho}\hbar = 978$eV. The number of photons per unit time and area is roughly $\frac{d}{da}\dot{N}_{ph} = \frac{15\sqrt{3}}{8}\frac{d}{da}P/E_c$, but not all of these photons an energy that is larger than the work function of niobium, i.e. 4.3eV.

Table 4 gives the total number of photons per Watt of radiation for the spectrum associated with three different magnet radii. Furthermore it specifies the fraction of these photons with an energy of less than the work function $WF$. This fraction has been computed by [8],

$$N_< = \int_0^{WF}\frac{dn}{dE}dE \ , \quad \frac{dn}{dE} = \frac{1}{\hbar^2\omega}\frac{dP}{d\omega} \ , \tag{22}$$

$$\frac{dP}{d\omega} = \frac{1}{\omega_c}S\left(\frac{\omega}{\omega_c}\right) \ , \quad S(x) = x\int_x^\infty K_{\frac{3}{2}}(\xi)d\xi \tag{23}$$

The relative number of photons below the energy $E$ is plotted in Fig. 11.

Assuming a quantum efficiency of $10^{-4}$, one can now compute the number of photons emitted per area when it is irradiated by 2kWm$^{-2}$. Since the synchrotron light

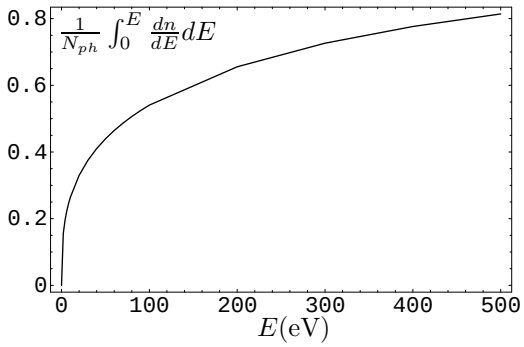


Figure 11: Number of photons below energy E, relative to the total number of photons for $\rho = 77$m.

arrives at the cavity approximately simultaneously with the electrons that created it, the photo-emitted electrons are accelerated away from the iris when a bunch in the energy recovery phase is passing the iris. Assuming these photons are focused without magnification onto the neighboring iris after gaining 2MeV of energy, the neighboring iris will obtain a sizable heat load due to this electron radiation. This heat load is shown in the last column.

| $\rho$(m) | $N_{ph}$(W$^{-1}$) | $\frac{N_<}{N_{ph}}$ | $\frac{dP_e}{da}$(kWm$^{-2}$) |
|---|---|---|---|
| 77 | $2.1 \cdot 10^{16}$ | 20% | 1.1 |
| 393 | $1.4 \cdot 10^{17}$ | 34% | 4.5 |
| 1291 | $5.8 \cdot 10^{17}$ | 49% | 11.3 |

Table 4: The electron radiation density due to photo emitted and accelerated electrons.

# 6 Reducing the Synchrotron Radiation: (a) By Shielding

The power densities of Figs. 6 and 7 are much higher than the 2kWm$^{-2}$ that are tolerable. The synchrotron radiation can be reduced in two ways: (1) by shielding the radiation using a collimator, and (2) by relaxing the bending radius of dipole magnets.

The shielding aperture is limited by the beam width, below which the high-energy particles of the order of a few GeV will hit the shielding material, resulting in undesirable scattering. Safety concerns force us to make the window width of the shield much wider than the beam width, ensuring that very few particles will hit the shield.

With the parameters of Tab. 1 and the Twiss parameters of [1], the standard deviations of the beam distribution are $\sigma_x = 0.0367$ mm and $\sigma_y = 0.0389$ mm. In our subsequent calculations, the horizontal aperture at the entrance of the first cavity was chosen to be $\pm$1cm, which is approximately $272\,\sigma_x$.

To get a rough estimate of the effectiveness of shielding, one can use Eq. (10) and solve for $x$ to find $x_{\min} = d/\Delta\phi - D - \frac{1}{2}\rho\Delta\phi$ as the first position to which radiation can be deposited. The first angle $\Delta\phi$ for radiation is given by Eq. (12) when $x$ and $d$ are replaced by the position $x_0$ and the half aperture $d_0$ of the collimator,

$$\Delta\phi_0 = \frac{D+x_0}{\rho}\left[\sqrt{1+\frac{2d_0\rho}{(D+x_0)^2}}-1\right], \quad (24)$$

$$\begin{aligned} x_{\min} &= \frac{d\rho - D(D+x_0)\left[\sqrt{\ldots}-1\right]}{(D+x_0)\left[\sqrt{1+\frac{2d_0\rho}{(D+x_0)^2}}-1\right]} \\ &\quad - \frac{\frac{1}{2}(D+x_0)^2\left[\sqrt{\ldots}-1\right]^2}{(D+x_0)\left[\sqrt{1+\frac{2d_0\rho}{(D+x_0)^2}}-1\right]} \\ &= \frac{(d-d_0)\rho}{(D+x_0)\left[\sqrt{1+\frac{2d_0\rho}{(D+x_0)^2}}-1\right]} + x_0 \\ &= \frac{d-d_0}{\Delta\phi_0} + x_0\ . \end{aligned} \quad (25)$$

For a collimator just before the linac ($x_0 = 0$) and a half aperture of 1cm one obtains $x_{\min} = 6.61m$. In reality, the collimator could never be so close to the cavity; here we use this location to get a lower limit on the radiation load. The radiation density on the cylindrical cavity wall as obtained from numerical propagation of radiation is given in Fig. 12. This result corresponds to the radiation bejond $x_{\min}$ in Fig. 6.

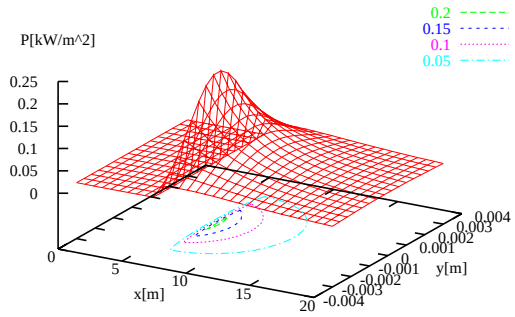


Figure 12: Radiation power density on cylindrical cavity surface, after shielding with an aperture of 1cm before the linac.

This radiation load would be tolerable, however, the worst case scenario with the rays hitting vertically to a screen at the distance 6.61 m is shown in Fig. 13.

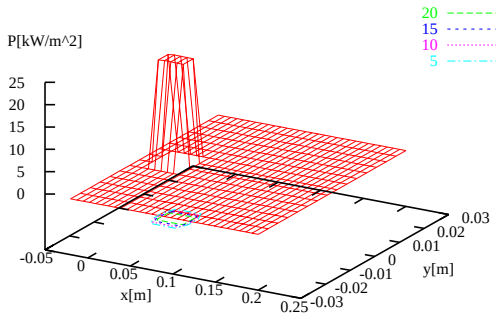


Figure 13: :Power density on a vertical screen at 6.61 m into the linac section after shielding with an aperture of 1cm before the linac.

# 7 Reducing the Synchrotron Radiation: (b) By Weakening Dipole Magnets

Due to the space constraints indicated in Fig. 1, we cannot blindly increase the bending radius of the dipole. We investigate two approaches to reduce the synchrotron radiation, while still having all the components fit roughly in the size of the original space.

## 7.1 Reduced Magnet Length

One way is to replace only a small section toward the end of the magnet with an elongated magnet with a larger bending radius. The radiation that shines into an aperture of radius $d_a = 1\,\mathrm{cm}$ from the dipole magnet at a distance $2.5\,\mathrm{m}$ ($x_0 = 0$) is due to less than the last $l = \rho\phi \approx 30\,\mathrm{cm}$ of the magnet. We can therefore reduce the length of this dipole and add a second dipole with substantially larger bending radius that creates the missing angle. This dipole should have just the right length so that only radiation from this dipole passes through the aperture and that $D_{\mathrm{new}}$ =80cm space is left between the dipole and the first cavity. The bending angle of the added dipole is determined by

$$\tan\Delta\phi = \frac{d_a + (\frac{D_{\mathrm{old}}-D_{\mathrm{new}}}{\sin\Delta\phi} + \rho_{\mathrm{old}})(1-\cos\Delta\phi)}{D + \rho_{\mathrm{old}}\sin\Delta\phi} \quad . \quad (26)$$

For the specified parameters, the new magnet is 2.11m long and has a bending radius of $\rho' = 393\,\mathrm{m}$. The resulting power per area on the cylindrical beam pipe is shown in Fig. 14, where the estimate of Eq. (16) was used. Note that now the first position in the linac that is reached by radiation is at $x_{\mathrm{min}} = 4.64\mathrm{m}$.

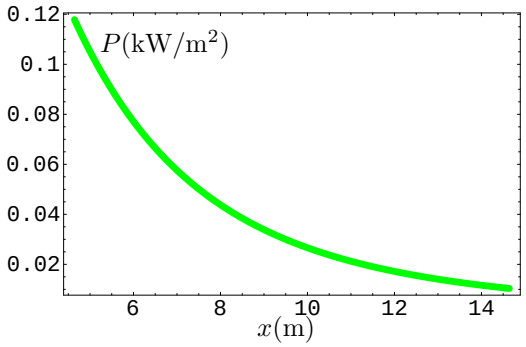


Figure 14: Estimated radiation density on the cylindrical cavity wall with a longer magnet and a radiation shield.

Using this estimate can be dangerous, however, since the finite width and divergence of the radiation source can cause radiation from the stronger magnet with $\rho = 77\mathrm{m}$ to radiate in the dipole. This causes the radiation density in Fig. 15 to be significantly larger close to $x_{mni} = 4.64\mathrm{m}$ than the estimate would suggest. To avoid this, the stronger magnet has to be reduced in length by slightly more than given by Eq. (26).

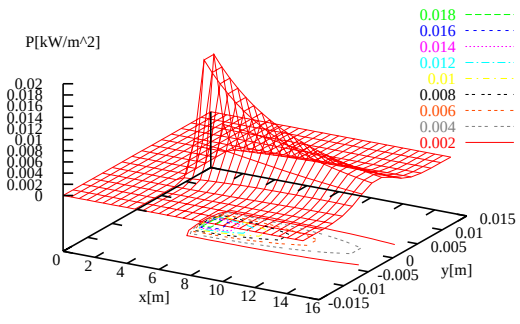


Figure 15: Radiation density on the cylindrical cavity wall with a longer magnet and a radiation shield, obtained by numerical radiation propagation.

While the radiation on the cylindrical surface is suitably small, the more realistic power density on the elliptical iris as shown in Fig. 16 is much larger than the tolarable $2\mathrm{kW/m^2}$.

## 7.2 Increase Magnet Strength

To reduce the radiation load below $2\mathrm{kWm^{-2}}$, further manipulations are necessary. One possibility is to increase the bending radius of the first part of the magnet, so that it becomes shorter and leaves more space for the second magnet with reduced strength.

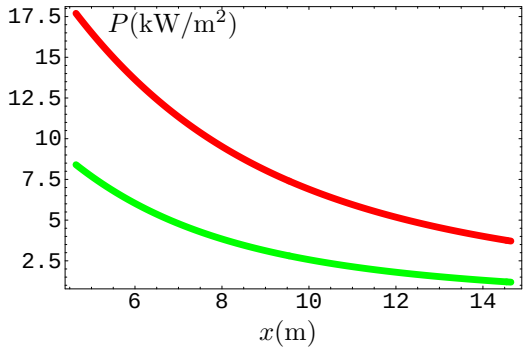


Figure 16: Power density on the elliptical iris. Computed for the first second iris (dark blue) and for an iris inside a multi-cell TESLA cavity (light green).

In the current design, the last dipole has a length of $l = 6\,\mathrm{m}$ with bending radius $\rho = 77\,\mathrm{m}$. The total angle covered by this dipole is $\phi = l/\rho \approx 78\mathrm{mrad}$. If we split this dipole into two parts and give the first part a radius of $\rho' = 45\,\mathrm{m}$, then it can cover the same angle in about $l = \rho'\phi = 3.51\,\mathrm{m}$, leaving $D = 4.99\mathrm{m}$ of drift space to the first cavity. The first angle that now shines through the aperture of $d_0 = 1\mathrm{cm}$ is determined by Eq. (24) to be $\Delta\phi = 2.0\mathrm{mrad}$. Equation (25) determines the first section in which the radiation reaches the surface to be at $x = 21.65\mathrm{m}$.

Analogous to the previous procedure we have to reduce the bending angle of the strong magnet by $\Delta\phi$ from Eq. (26) and we have to add a $l' = 4.34\mathrm{m}$ long magnet with $\rho' = 1291\,\mathrm{m}$. Ignoring the space between the two magnets, this again leaves a drift space of $D = 0.8\mathrm{m}$.

The radiation density which this scheme produces on the cylindrical cavity wall and on the elliptical irises is shown in Figs. 17 (top and bottom). Note that now the first position in the linac that is reached by the radiation is at $x = 7.43\mathrm{m}$.

While this radiation load seems acceptably small, it has to be remembered that a 6 times larger power from photo-emitted electrons can be expected as shown in Tab. 4.

### 7.3 Other Collimation Strategies

To limit the power load, it seems necessary not only to shield the entrance of the linac, but to reduce the aperture of the higher order mode ferrite dampers to cast a shadow on each cavity, or to put other x-ray collimators inside the linac at appropriate positions. For this purpose, it would be suitable to locate the last dipole in such a way that the complete fist cryomodule of about 15m length is not irradiated. A second collimator after this cryomodule would then cast an even longer shadow

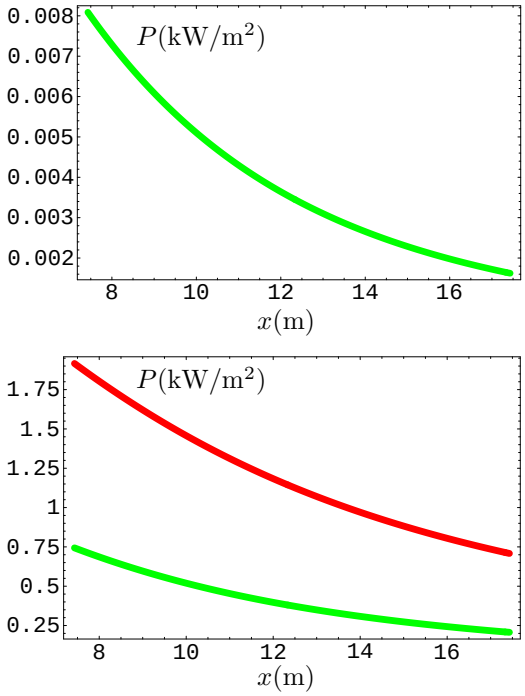


Figure 17: **Top**: Estimated radiation density on the cylindrical cavity wall with one stronger and one longer magnet and a radiation shield. **Bottom**: The more realistic power density on the elliptical iris.

along the linac. For example, one can place the last magnet with $\rho = 77\mathrm{m}$ about 6m before the linac. An aperture of 1cm would then cast a shadow of 16.16m on the cavity walls. A similar collimator after a 15m long first cryomodule would then cast a shadow to 52.55m inside the linac. A 1cm aperture after the fourth cryomodule at 60m into the linac would finally bring the total 140m long linac section of Fig. 1 into the shadow.

## 8 Conclusion

The power density due to x-rays or photo-electrons hitting a superconducting niobium surface in a 2K helium bath must be limited to $2\mathrm{kWm^{-2}}$. Achieving this in the suggested ERL in the CESR tunnel will require many changes of the dipole arrangements as well as significant collimation of the synchrotron fan before entering the linac section. This first analysis shows that these measures can lead to a reduction of the radiation to about $700\mathrm{Wm^{-2}}$ for the incoherent radiation. The resulting power due to photon-emitted electrons can however be significantly larger. The power from coherent radiation can be much higher, but it is in the infrared range and is therefore reflected strongly and therefore is distributed over the complete cavity surface.

Several questions remain, however: (a) What x-ray and particle radiation are created in the collimation process, and how do they disturb the superconducting cavities? (b) Can reflections of synchrotron radiation that is created upstream of the end of the last magnet be suppressed sufficiently? (c) Can a photo-emitted current be undesirably focused in a way that the high power densities would damage the chamber walls?

# 9 Acknowledgments

We would like to thank Dave C. Sagan for providing instructions on how to use the BMAD program. This work was funded by Cornell University.

# References

[1] G. H. Hoffstaetter, I. Bazarov, D. Sagan, R. Talman, Proceedings of PAC'03, Portland (May 2003)

[2] M. Seidel, The Upgraded Interaction Regions of HERA, Report DESY-HERA-00-01 (2000)

[3] Klaus Wille, The Physics of Particle Accelerators, Oxford University Press (2000)

[4] BMAD lattice program, maintained by David Sagan, Laboratory of Nuclear Studies, Cornell University (2003)

[5] TESLA Technical Design Report, Report DESY (1995)

[6] Grigorii Eremeev, Cornell University, private communication (2003)

[7] Phase I Energy Recovery Linac (ERL) Synchrotron Light Source at Cornell University, Report Cornell CHESS-01-003 (2001)

[8] Matthew Sands, The Physics of Electron Storage Rings, Report SLAC-121 and UC-28 (ACC) (1970)

[9] Terahertz Wakefields in the Superconducting Cavities of the TESLA-FEL Linac, Report DESY (March 2000)